Model of Gas Flow Through Porous Refractory Applied to an Upper Tundish Nozzle

RUI LIU and BRIAN G. THOMAS

Argon gas commonly is injected into the liquid metal stream through the porous refractory walls in many metallurgical processes. In this work, a new model has been developed to investigate gas diffusion through heated porous refractory, including the effects of refractory geometry, the thermal expansion of the gas, temperature-dependent gas viscosity, and possible leakage into unsealed joints. A novel one-way-flow pressure boundary condition has been formulated and implemented to prevent unrealistic flow into the refractory. The complete model is validated with both analytical solutions of 1D test problems and observations of a water bubbling experiment. Then, to demonstrate practical application of this general model, argon gas flow is simulated through a double-slitted upper tundish nozzle during continuous steel casting with a slide-gate system. Realistic liquid steel pressure distributions with the bubbling threshold condition are applied on the inner surface. Parametric studies are conducted to investigate the effects of joint gas leakage, refractory conductivity, permeability, and injection pressure on the resulting gas distributions, gas mass flow rates, and leakage fraction. This new model of porous flow can serve as the first step of a comprehensive multiphase model system.

DOI: 10.1007/s11663-014-0198-5

I. INTRODUCTION

ARGON gas is widely used in metallurgical processes for many purposes, such as gas injection through a porous plug to stir the ladle, gas injection to remove inclusions in the tundish, and gas injection through the upper tundish nozzle (UTN) during continuous casting to prevent reoxidation and nozzle clogging[1] as shown in Figure 1.[2] This injected gas significantly affects flow in these vessels, and may be detrimental if not properly controlled. Extensive research has investigated gas–liquid two-phase interactions in those vessels (*e.g.*, ladle,[3–6] tundish,[7,8] and continuous casting[9–14]), *via* physical and mathematical modeling. Physical models provide qualitative understanding of the gas–liquid two-phase interactions and can be used to validate computational models. However, physical model results from an air–water system differ from an otherwise similar argon–metal system due to some differences in material properties (*e.g.*, surface tension and density) and in operation conditions (*e.g.*, temperature gradient) between these two systems.[10] Thus mathematical modeling becomes a necessary tool to study gas–metal two-phase flows in commercial processes. Computational models have been applied extensively to study argon gas effects on steel continuous casting using mixture models,[10,14] Eulerian–Eulerian models[9,11] and Eulerian–Lagrangian models.[12,13] The accuracy of these modeling efforts depends on two key parameters: the volumetric flow rate of argon gas entering the steel in the hot condition, and the initial bubble size distribution. Both parameters have been investigated in previous work.[10,14,16]

The volumetric flow rate of the injected argon gas is usually measured in the "cold", standard temperature and pressure (STP) condition well before entering the nozzle, in standard liters per minute (SLPM). This is usually much smaller than the flow rate entering the molten metal in hot condition through refractory walls, due to gas thermal expansion. This effect is accounted for with the ideal gas law, as implemented in Reference 10 to estimate volumetric flow rate in the hot condition exiting the SEN port during continuous casting:

$$Q_{\mathrm{g,hot}} = Q_{\mathrm{g,cold}} \left(\frac{T_0}{T_\infty} \right) \left(\frac{p_\infty}{p_\infty + \rho g L_{\mathrm{n}}} \right), \qquad [1]$$

where Q_{g} is the gas flow rate (m^3/s), T_0 is the casting temperature (K), T_∞ is the ambient temperature (K), p_∞ is the ambient pressure (Pa), and L_{n} is the pressure head of molten steel above the gas injection region (m). This calculated gas flow rate in the "hot" condition is then used to find the bubble size distribution and is applied as the inlet boundary condition for the gas phase in two-phase flow simulations.

This simple model relies on two basic assumptions: (1) no gas leakage, and (2) uniform pressure and temperature distributions at both the gas injection and exit surfaces. However, these two assumptions are not usually satisfied in real-world applications. Some of

RUI LIU, formerly Ph.D. Student with the Department of Mechanical Science and Engineering, University of Illinois at Urbana-Champaign, 1206 West Green Street, Urbana, IL 61801, is now Process Research Engineer with ArcelorMittal, Inc. Global R&D, East Chicago, IN. BRIAN G. THOMAS, Gauthier Professor, is with the Department of Mechanical Science and Engineering, University of Illinois at Urbana-Champaign. Contact email: bgthomas@illinois.edu
Manuscript submitted February 11, 2014.
Article published online October 3, 2014.

the gas escapes through leaks in the delivery system, cracks in the refractory or imperfect seals at the joints between refractory components. The remaining gas expands as it travels through the heated refractories and enters the steel flow with a non-uniform distribution. Operators can identify extreme leakage by the drop in the measured "back pressure" of the gas.[15]

The bubble size distribution in the molten metal that results from gas injection is also important but difficult to determine. Iguchi *et al.*[16,17] performed experiments with vertical gas injection into stagnant liquid in both mercury–air[16] and iron–argon systems[17] under relatively large gas flow rates (20 to 400 ml/s), and developed empirical correlations to predict gas bubble sizes under different operating conditions. Bai and Thomas[18] developed a semi-analytical two-stage model to predict initial bubble formation from a single hole in the nozzle wall, considering the important drag effect of the downward-flowing steel. They calibrated and validated this model to reproduce measurements in air–water systems, and applied it to predict the bubble size entering into argon–steel flow systems. Ghaemi *et al.*[19] recently measured the size distributions of microbubble formation upon entering a water channel with cross flow, taking into account the effects of the gas injector locations and also the bubble coalescence (termed secondary bubble formation) at high gas flow rates. Empirical correlations were generated to predict initial and secondary bubble sizes.[19]

Little experimental work has been conducted to study gas flow through porous refractory and to investigate the bubble size distributions that exit the refractory surface to enter the liquid. Kazakis *et al.*[20] injected air through metal spargers into initially stagnant water and measured the bubble size distributions. A correlation to predict the mean bubble size based on dimensionless groups including Froude (*Fr*), Weber (*We*), and Reynolds (*Re*) numbers was obtained from the air–water measurements.[20]

In addition to the gas flow rate and pressure distributions, the prediction of bubble size distribution depends on quantifying the number density of "active sites"[21] through which gas streams leave the porous refractory surface. Previous work[22,23] has found that the number of active sites per unit area (#/cm^2) is much fewer than the total available sites, and increases with increasing gas flow rate, and decreases with surface tension and gas viscosity. In addition, the number of active sites depends on the specific permeability and porosity of the refractory,[23] contact angle,[23] cross-flow velocity,[23] and liquid density.[22]

Difficulties arise in correlating the gas flow rates and bubble size measurements in water models with those in metallurgical processes, due mainly to the great

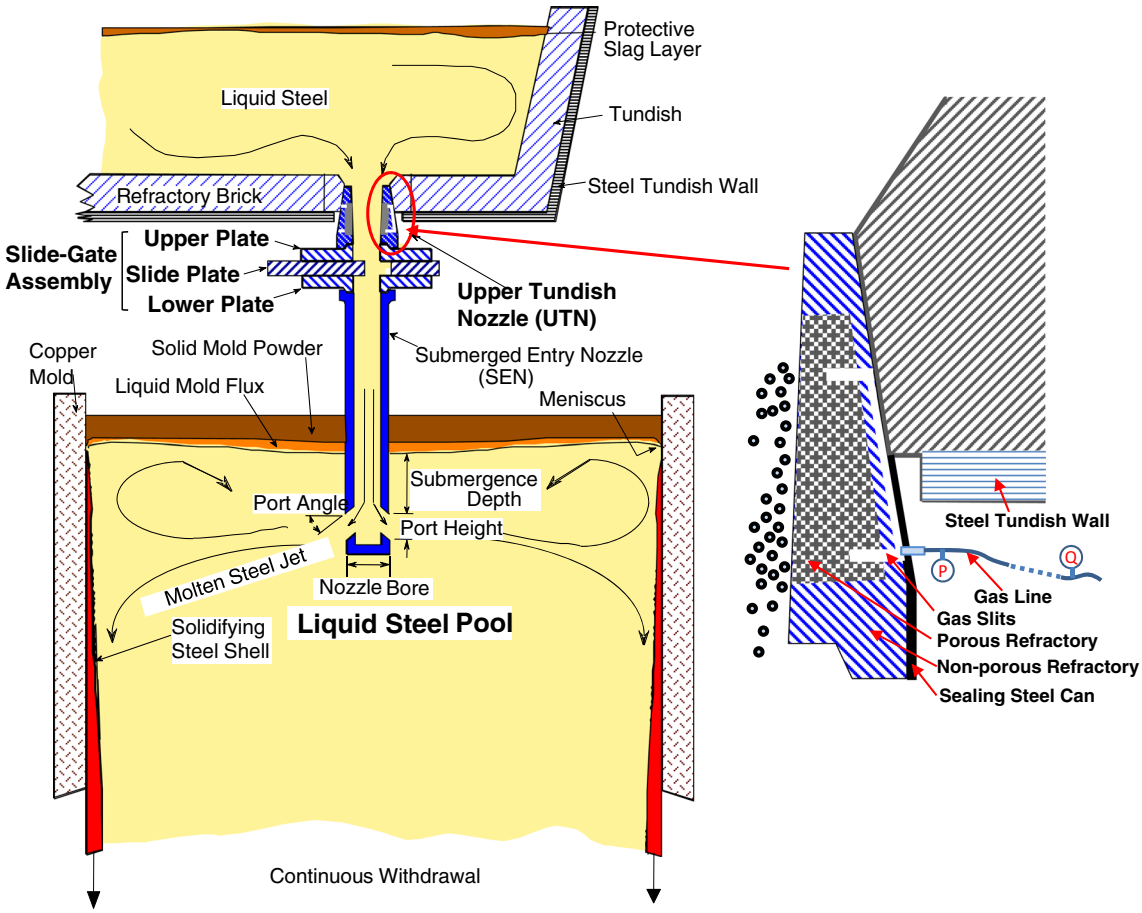

Fig. 1—Schematic of upper tundish nozzle (UTN) and continuous casting process.

differences in temperature gradients and surface tension between the air–water and argon–steel systems.[16,17] Also, to predict a reasonable initial bubble size distribution, the realistic, non-uniform distribution of the superficial (average) velocity of the gas exiting the refractory-liquid interface is needed, which cannot be obtained from experiments.

Thus a model is needed to predict realistic distributions of gas flow and velocity inside the porous refractory, taking into account the effects of non-uniform pressure and temperature, complicated geometry, refractory, gas, and interfacial properties, and joint sealing conditions, during bubble formation. In this work, new models and boundary conditions are developed to investigate these phenomena. After validation with both analytical solutions and experimental observations, the models are applied in a brief parametric study, and extensions to predict bubble size and gas leakage detection are discussed.

II. MATHEMATICAL MODEL DESCRIPTION

To model gas flow through a heated porous medium, the porous flow equations must be coupled with heat transfer and mass conservation to account for gas thermal expansion and temperature-dependent viscosity. To implement realistic boundary conditions, in this work, the pressure distribution of liquid metal surrounding porous refractory is calculated *via* Bernoulli's equation. In addition, a pressure threshold with a novel one-way flow condition is derived to account for interfacial tension effects during bubble formation at pore exits on the partially wetted surface of porous refractory. A general-purpose methodology to simulate gas flow through heated porous refractory is presented in the following sections.

A. *Governing Equations*

Two independent models are developed here to simulate gas flow through a porous medium: a pressure-source model, and a complete porous-flow model. To incorporate the thermal expansion effect, a steady-state heat conduction equation was first solved to calculate the temperature distribution within the nozzle refractory walls:

$$\nabla \cdot (k \nabla T) = 0. \quad [2]$$

The gas density ρ is given by the ideal gas law:

$$\rho = p/(RT), \quad [3]$$

where R is the specific gas constant for argon, (207.85 J kg^{-1} K^{-1}), p is absolute gas pressure (Pa), and T is absolute temperature (K).

To satisfy mass conservation, the following continuity Eq. [4] is solved in both models, which retains gas density because it is compressible and also varies due to thermal expansion,

$$\nabla \cdot (\rho \mathbf{v}) = 0, \quad [4]$$

where $\mathbf{v}$ is the superficial (average) velocity vector of the gas flowing inside the porous refractory. The actual local velocity is much larger, depends on pore size, and is calculated from the results of this work only at the surface, knowing the number of active sites.

1. *Porous-flow model*

For the porous-flow model, the steady-state Navier–Stokes equations [5] are solved in three dimensions for the superficial gas velocities and pressure distribution with two additional momentum sink terms to simulate flow through porous media:

$$\rho \mathbf{v} \cdot (\nabla \mathbf{v}) = -\nabla p + \nabla \cdot (\mu \nabla \mathbf{v}) - \left(\frac{1}{K_D} \mathbf{v} + C \frac{1}{2} \rho |\mathbf{v}| \mathbf{v} \right). \quad [5]$$

The two extra sink terms in the brackets on the right-hand-side of Eq. [5] are first, for viscous momentum loss, and second, for inertial momentum loss, which is neglected in creeping flows ($Re < 1$) by setting C to zero.[24] When inertia is important, C could be measured from permeability tests[25] or calculated from models.[26]

The permeability of gas flow through a porous medium, K_D, is defined as the ratio of two properties, as shown in Eq. [6]: the specific permeability K_{DS} of the refractory, and the dynamic viscosity μ of the gas, which varies greatly with temperature:

$$K_D = \frac{K_{DS}}{\mu(T)}. \quad [6]$$

Here, K_{DS} is the refractory specific permeability, which is assumed to be isotropic in this work, and is given a typical value of 1.01×10^{-12} m^2,[27] which also falls in the range of previous measurements.[23] The specific permeability denotes the flow resistance of the porous refractory material, which depends on the pore structure connectivity of the porous medium, and does not depend on temperature, because solid thermal expansion effects on the pore structure are negligible.[28]

2. *Pressure-source model*

The transition from diffusion to momentum-dominated flows in porous media (in both consolidated and unconsolidated cases) was found to start at a Re between 1.0 and 10, defined as[29,30]:

$$Re = \frac{Q \rho \delta}{\mu A \phi}, \quad [7]$$

where Q is the fluid volumetric flow rate, ρ is fluid density, μ is dynamic viscosity, δ is the average pore diameter, A is the sample cross-section area, and ϕ is porosity. When the flow is laminar with low gas velocities, only the viscous resistance (Darcy's law) is needed to describe the flow in porous media. This is the situation in most cases of gas injection into liquid metal through porous refractories in metallurgical processes. Because the pores and flow rates are very small, flow is laminar over a wide range of ceramic refractory

materials.[28] For instance, for gas injection through UTN during continuous casting process, the typical Reynolds number of gas flow in the porous refractory calculated *via* Eq. [7][29] is around 10^{-2}, which is much smaller than 1, so inertia is negligible. In this scenario of laminar gas flow, a simple "pressure-source" model is developed by adopting Darcy's law to obtain gas velocity distribution from local pressure gradient:

$$\mathbf{v} = -K_D \nabla p. \qquad [8]$$

Re-organizing Eqs. [3], [4], and [8] gives Eq. [9], which is the final form of the equation solved in the "pressure-source" model.

$$\nabla \cdot (K_D \nabla p) = -\frac{RT}{p}\left[\nabla\left(\frac{p}{RT}\right) \cdot (K_D \nabla p)\right]. \qquad [9]$$

The left side of the Eq. [9] is a pressure diffusion term, and the right side contains two source terms to account for thermal expansion of the gas and the permeability (gas viscosity) change with temperature. This nonlinear elliptic equation can be solved with a simple Poisson equation iterative solver (same form as steady heat conduction with nonlinear heat sources), so is easy to program with an in-house code. This pressure-source model reveals the fundamental phenomena that govern the gas flow, is easy to solve using a heat-conduction solver for example, and has useful analytical solutions. However, it loses accuracy when high superficial gas velocities are generated in the porous refractory (*e.g.*, $Re \gg 1.0$) and inertial effects become important. In such cases, the porous-flow model would be more accurate.

B. *Boundary Conditions*

The boundary conditions for the computational model include convective boundary conditions for the heat transfer analysis, pressure Dirichlet boundary conditions for the pressure injection slits (and exposed refractory area), zero normal-velocity conditions at sealed interfaces, and a novel pressure boundary condition to ensure one-way gas flow at the refractory-metal interface. Combining all of these boundary conditions enables the model to make realistic predictions for practical applications.

1. *Heat transfer model boundary conditions*

The boundary conditions on the heat transfer Eq. [2] depend on convection between the refractory and the surrounding flowing fluids. A convective boundary condition is applied at both the inner UTN surface contacting the liquid metal, and the outer surface surrounded by ambient air. The heat transfer coefficients, tabulated in Table II, are calculated using the following *Nu* number correlation from Sleicher and Rouse[31]:

$$h = \frac{Nu \cdot k}{D}, \quad Nu = 5 + 0.015 Re^a Pr^b, \qquad [10]$$

where $a = 0.88 - \left(\frac{0.24}{4+Pr}\right)$, and $b = \frac{1}{3} + 0.5\exp(-0.6Pr)$, with $Pr = \frac{\mu}{\rho\alpha}$, and $Re = \frac{\rho UD}{\mu}$.

It is also important to note that the gas permeating through the micro-channels in the refractory quickly heats up to the local temperature of the UTN.[9] So a "one-way" coupling of the heat transfer model results to the gas flow model is adopted. This is another reasonable assumption of the current model.

2. *Flow model boundary conditions*

The boundary conditions for the porous gas flow simulations are an essential part of the model for realistic gas distribution and gas leakage predictions. On the surfaces of the vertical-channel and annular-shaped distribution slits in the refractory, the gas injection pressure is fixed:

$$p = p_{\text{inject}}. \qquad [11]$$

The interfaces between the refractory and the outer steel can are assumed to be perfectly sealed to prevent any leakage, so also have zero normal gas flow, which is imposed in the porous-flow model as follows.

$$\mathbf{v} \cdot \mathbf{n} = 0, \qquad [12]$$

where $\mathbf{n}$ is the outward-normal direction vector at the appropriate domain boundary. The following equivalent condition is imposed to prevent normal flow for the pressure-source model:

$$-K_D(\nabla p)_b \cdot \mathbf{n} = -K_D\left(\frac{\partial p}{\partial n}\right)_b = 0. \qquad [13]$$

On symmetry planes, this "no penetration" condition must again be applied, which is equivalent to a Neumann B.C.[32] for pressure, with zero surface-normal pressure gradient, as given in Eqs. [12] or [13].

For refractory surfaces that are exposed to the surrounding environment, the ambient pressure is used as the boundary condition, given by:

$$p = p_{\text{ambient}}. \qquad [14]$$

At joints between refractory pieces, both the sealed-bottom and open-bottom cases are explored, and boundary conditions in Eqs. [13] and [14] are adopted, respectively, for these two cases.

3. *Refractory-metal interface*

The interface between the porous refractory and the liquid (metal) is where the most influential boundary condition of the model must be applied. For gas to exit the refractory-liquid interface into the liquid bulk, a pressure jump is needed to overcome the surface tension force in order to curve the interface, form, and detach bubbles. This pressure jump Δp is a "bubbling" threshold that can be calculated following the Young–Laplace equation[33] as:

$$\Delta p = p_b - p_l = \sigma\kappa = \frac{2\sigma}{r_{\text{pore}}}, \qquad [15]$$

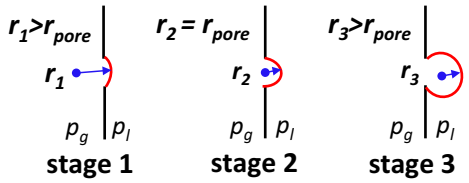

Fig. 2—Bubble formation stages at refractory surface showing expansion and pressure threshold (stage 2).

where p_b is gas pressure p at the refractory interface (or boundary), p_l is liquid pressure at the interface, σ is the surface tension, κ is the curvature of the gas at the refractory-liquid interface, and r_{pore} is the effective radius of the active refractory pore, where the gas exits. This quantifies how the liquid pressure is less than the pressure of the gas inside the refractory.

Figure 2 illustrates the stages of bubble formation. At the initial stage 1, less than a half of a spherical bubble surface intrudes into the liquid and the radius of the bubble cap is larger than that of the pore opening, resulting in a small curvature. At stage 2, the hemisphere bubble diameter equals the pore diameter which defines the maximum curvature. At the third stage, the bubble has expanded beyond the hemisphere shape, with a larger diameter and less curvature.

The pressure jump is governed by the maximum bubble surface curvature, which occurs at the second stage. The pressure jump threshold also governs flow entry into the refractory pores from the liquid metal. Kaptay *et al.*[34] studied this "liquid penetration" phenomenon experimentally and tabulated the pressure threshold for liquid to enter the porous refractory and the maximum penetration depth. A capillary pressure balance needs to be considered to predict this maximum liquid penetration depth, which includes the triple point contact angle between the liquid, gas, and refractory inside the pore, in addition to the pore diameter. During continuous casting, this threshold pressure for liquid steel penetration is around 42 kPa, for a pore diameter of 100 μm and a contact angle of 150 deg.[35] Considering the low liquid pressures that accompany gravity-driven flow, this result implies that the liquid steel should never enter the UTN refractory in metallurgical processes with typical gas injection pressures.

Based on the discussions above, the boundary condition at the refractory-liquid interface must serve two different scenarios: when gas pressure near the interface exceeds the pressure threshold for bubble formation, the boundary pressure should equal the sum of the local liquid-steel pressure and the bubbling pressure threshold; when the gas pressure is smaller than the bubbling pressure barrier, the boundary should be considered "sealed" as no liquid steel penetrates into the refractory and no gas exits the local refractory pores. The latter zero-penetration velocity boundary condition can also be satisfied by applying Eq. [13].

In this work, a novel Robin-type[32] (or mixed) boundary condition, is developed to satisfy the two requirements of the previous discussion, by enforcing the following equation set for one-way flow at the refractory-liquid interface:

$$\begin{cases} \text{if} \left(\frac{\partial p}{\partial n}\right)_b < 0, & p_b = p_l + \frac{2\sigma}{r_{pore}} \\ \text{else}, & \left(\frac{\partial p}{\partial n}\right)_b = 0 \end{cases}, \qquad [16]$$

where p varies with distance along the interface boundary (subscript b). This equation seals portions of the boundary, which are unknown prior to the calculation. The choice of Dirichlet (first) or Neumann (second)[32] boundary condition case in Eq. [16] is part of the model solution. Clearly, an iterative method is needed for this purpose, as discussed later.

C. *Liquid Pressure Model*

The boundary condition, Eq. [16] requires p_l, which depends on the behavior of the liquid outside of the refractory domain. However, the pressure distribution in the liquid metal usually cannot be measured directly in the metallurgical vessels, and may be difficult to obtain. Sometimes, such as in a ladle porous plug, this pressure can be considered a constant as the hydrostatic pressure. In other situations, such as beneath a stopper rod, a full computational model of the turbulent fluid flow of the liquid steel should be applied. In this work, a simple model to find p_l with vertical distance down the UTN wall was developed using Bernoulli's equation, based on balancing potential and kinetic energy of the fluid flow:

$$p(z) = p_0 + \rho_l g(h_{tundish} + h_{UTN} - z) - \frac{1}{2}\rho_l U^2, \qquad [17]$$

where p_0 is the pressure at tundish level (atmospheric pressure), g is gravitational acceleration, $h_{tundish}$ and h_{UTN} are heights of the tundish level and UTN, respectively, U is mean velocity at any UTN cross-section, and z is the distance above the UTN bottom. This equation is reasonable for any distance above the slide plate, below which the pressure drops due to the sudden contraction of the flow area) and U increases in a non-uniform manner.

D. *Material Properties*

The permeability depends on both the pore structures of the consolidated refractory, and the dynamic viscosity of the gas, μ, which varies greatly with temperature. Thus, in metallurgical processes involving large temperature gradients, the gas viscosity and permeability are coupled with the temperature field. Incorporating anisotropic, temperature-dependent specific permeability, and non-uniform pore size distribution into the current model is straight forward. Lacking such property measurements, this work assumes isotropic, temperature-independent specific permeability, and uniform pore size. The argon gas viscosity is taken from measurements[36]:

$$\mu(T) = \mu_0 \times 10^{\left(0.63842 \log_{10} T - 6.9365/T - 3374.72/T^2 - 1.51196\right)}, \quad [18]$$

where μ_0, 2.228 × 10^{-5} Pa s, is the dynamic viscosity at 293 K (20 °C).

Thermal conductivity of the refractory for the base case is 18 W/(mK). The surface tension between the liquid steel and argon gas is 1.157 N/m, which is about 16 times that of the water–air system.[18] A typical specific permeability of 10.1 npm is chosen for the base case, taken from measurements on a medium-permeability refractory with 17 pct porosity.[23,37] For a parametric study, this specific permeability is varied between 2.0 and 12.0 npm.

E. *Numerical Details*

Owing to the one-way coupling of this system, the energy Eq. [2] is first discretized using a finite-volume method and solved for the temperature field, followed by solving for the pressure and velocity fields. For the porous-flow model, the coupled ideal gas law and momentum Eqs. [3] through [5] were discretized using the third-order MUSCL scheme[38] and solved using the SIMPLE algorithm[39] in Fluent by ANSYS Inc.[24] For the pressure-source model, Eq. [9] was similarly discretized and solved for pressure as a user defined scalar (UDS) in ANSYS Fluent,[24] with the nonlinear source term right side of Eq. [9] implemented in a user defined function (UDF). Velocities are then computed from the pressure field using Eq. [8]. The system converges easily with any solution strategy.

The one-way flow pressure boundary condition is applied in an iterative process. At the beginning of each new iteration $i + 1$, a pressure is prescribed at the local boundary face according to the evaluation of conditions in Eq. [16], based on the known pressure distribution from previous iteration, i, *via* Eq. [19] below:

$$\begin{cases} \text{if } \left(\frac{\partial p}{\partial n}\right)_{\text{b}}^{i} < 0, & p_{\text{b}}^{i+1} = p_{\text{l}} + \frac{2\sigma}{r_{\text{pore}}} \\ \text{if } \left(\frac{\partial p}{\partial n}\right)_{\text{b}}^{i} \geq 0, & \left(\frac{\partial p}{\partial n}\right)_{\text{b}}^{i+1} = 0 \end{cases}. \quad [19]$$

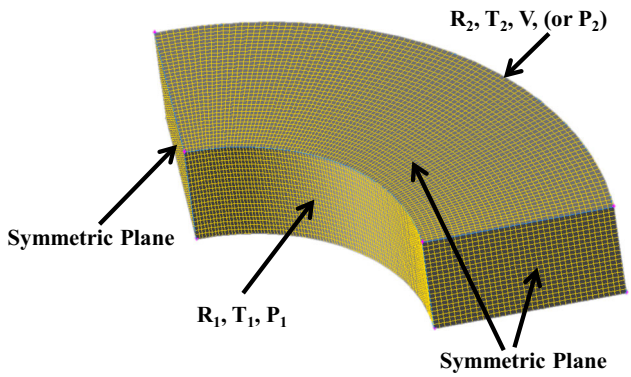

Fig. 3—Geometry, mesh, and boundary conditions for 1D test cases.

The Dirichlet case in Eq. [19] is straight forward to apply. The zero pressure gradient condition normal to the surface is achieved by setting the pressure on the local surface, according to Eq. [20], which is derived from the zero diffusion flux boundary condition for an unstructured mesh in finite-volume formulation from Mathur and Muthy[40] and adopted in Ansys Fluent,[24] to account for non-orthogonal boundary cells.

$$p_{\text{b}} = p_{\text{c}} + d_{\text{b}} \left[(\nabla p)_{\text{c}} \cdot \mathbf{e}_{\text{b}} - (\nabla p)_{\text{c}} \cdot \mathbf{A}_{\text{b}} \frac{\mathbf{A}_{\text{b}} \cdot \mathbf{e}_{\text{b}}}{\mathbf{A}_{\text{b}} \cdot \mathbf{A}_{\text{b}}} \right], \quad [20]$$

where subscript c represents the cell adjacent to the current boundary face (with subscript b); $\mathbf{e}_{\text{b}}$ is a vector from the cell centroid to the geometric center of the boundary face with magnitude equal to the distance, d_{b}; "area vector" $\mathbf{A}$ is a vector perpendicular to the cell boundary face with magnitude equal to the face area. If vectors $\mathbf{e}_{\text{b}}$ and $\mathbf{A}$ are parallel (indicating that the cell is orthogonal), then Eq. [20] simplifies to $p_{\text{b}} = p_{\text{c}}$. Further computational details are presented elsewhere[40,41] and in later sections.

III. MODEL VALIDATION

Two separate test problems related to steel processing were used to validate the models described in the previous section: (1), a simple one-dimensional problem with analytical solution, and (2) a real bubbling experiment in a submerged commercial UTN.

A. *Comparison with 1D Analytical Solutions*

The first test problem is one-dimensional cylindrical flow of argon gas, which is injected into the outer-radius surface of a round refractory pipe, and exits from the inner-radius surface. Figure 3 shows the computational domain of one quarter of a short segment of the pipe, and boundary conditions investigated for this test problem. The mesh contains 60,000 hexahedral cells in a Cartesian coordinate system. The problem is solved numerically in three dimensions, with both the pressure-source model and the porous-flow model.

The governing Eqs. [2] and [9] simplify to the following coupled ordinary differential equations (ODEs) in a cylindrical coordinate system with respect to radial position, r,

$$\begin{cases} \frac{1}{r}\frac{\mathrm{d}}{\mathrm{d}r}\left(r\frac{\mathrm{d}T}{\mathrm{d}r}\right) = 0 \\ \frac{\mathrm{d}^2 p}{\mathrm{d}r^2} + \frac{1}{r}\frac{\mathrm{d}p}{\mathrm{d}r} = \left(\frac{1}{T}\frac{\mathrm{d}T}{\mathrm{d}r} - \frac{1}{K_{\text{D}}}\frac{\mathrm{d}K_{\text{D}}}{\mathrm{d}r}\right)\frac{\mathrm{d}p}{\mathrm{d}r} - \frac{1}{p}\left(\frac{\mathrm{d}p}{\mathrm{d}r}\right)^2 \end{cases}. \quad [21]$$

The outer surface boundary condition is either specified pressure p (case 1) or specified velocity V (case 2). The inner-radius surface has constant absolute pressure of 100 kPa as boundary condition in both cases. The inner and outer surface temperatures are fixed at T_1 and T_2, respectively. The two side walls and the top and bottom walls of the numerical model are set to symmetry planes. The parameters, tabulated

Table I. Parameters for 1D Test Case Boundary Conditions (Based on Absolute Pressure)

R_1 (m)	R_2 (m)	P_1 (kPa)	P_2 (kPa)	T_1 [K (°C)]	T_2 [K (°C)]	V (m/s)
0.0375	0.0725	100	200	1800 (1527)	1000 (727)	0.0073

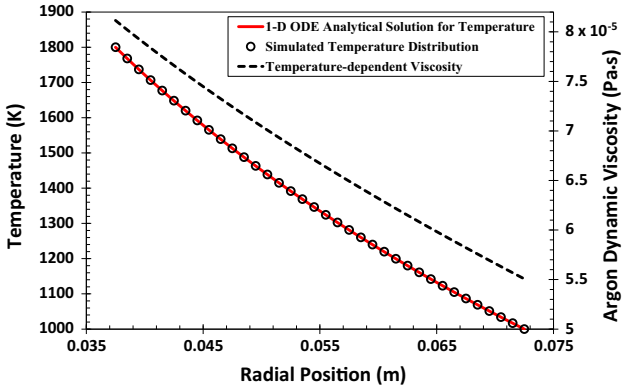

Fig. 4—Temperature and argon viscosity profiles in radial direction.

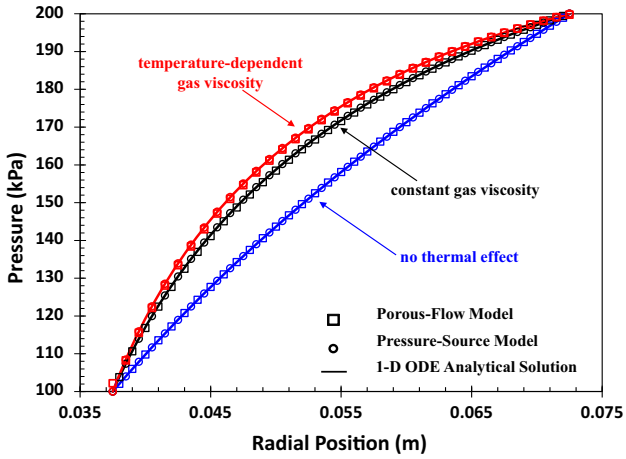

Fig. 5—Pressure distributions for 1D test cases with fixed pressure B.C..

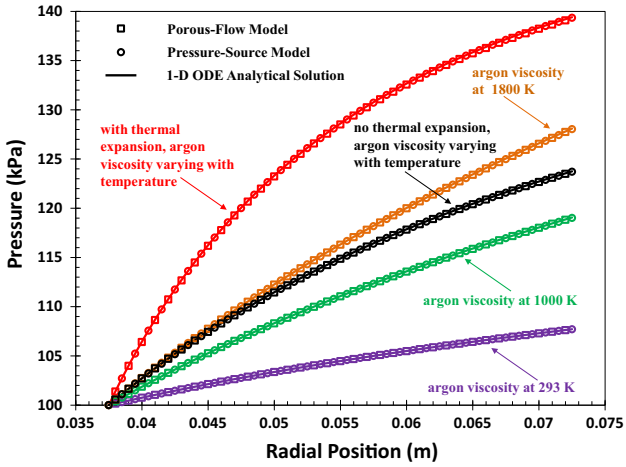

Fig. 6—Pressure distributions for 1D test cases with fixed gas mass flow rate B.C..

in Table I, are chosen to approximate realistic operating conditions of a typical UTN during continuous casting.

In both case 1 and case 2, three different scenarios are considered to study the effects of temperature-dependent gas viscosity and gas compressibility: (1) without any thermal effects; (2) with thermal expansion and constant gas viscosity; and (3) with thermal expansion and a realistic temperature-dependent gas viscosity. The numerical simulation results are compared with the analytical solutions derived in Appendix A.

The temperature solutions are compared in Figure 4, which also shows the realistic gas viscosity profile. The radial heat flow causes a slight deviation from a linear temperature profile, and the numerical simulations of this simple problem are exact to within 0.02 pct (based on L2-norm[32]).

Pressure results from using the fixed pressure boundary condition are shown in Figure 5, for the three different scenarios, and compared with their respective analytical solutions. Three curves each are presented for the porous-flow model, (squares), the pressure-source model (circles), and the 1D analytical solutions, (lines). For all three cases, the pressure-source model and porous-flow model match perfectly with each other, and with the analytical solutions. Thus all three models are validated. Thermal expansion and temperature-dependent gas viscosity both produce higher pressures everywhere within the nozzle. Without thermal effects, the pressure distribution is almost linear, with slight upward curvature caused by the surface area difference between the inner and outer surfaces of the curved refractory walls.

Pressure distributions with the fixed argon mass-flow-rate (velocity) boundary condition are shown in Figure 6. Again, the two numerical models and the analytical solution all agree almost exactly for each of the five scenarios tested, providing further model validation. To achieve the same gas flow rate at the outer surface, the pressure inside the wall must increase to overcome three different effects which combine together, in order of importance: thermal expansion of the gas, increasing gas viscosity with temperature, and difference between inner and outer tube diameters. Increasing temperature towards the inside-radius tube bore causes the gas to expand, and the gas viscosity to increase. Results for constant gas viscosities at three different temperatures [293 K, 1000 K, and 1800 K (20 °C, 727 °C, and 1527 °C)] show that increasing gas viscosity lowers the permeability, which requires a higher injection pressure to enforce the same gas flow rate. Finally, the smaller area of the inner surface requires a higher pressure to push the same amount of gas through the inner surface of the refractory into the liquid, relative to a flat wall.

B. *Comparison with UTN Bubbling Experiment*

The second test problem is a bubbling experiment, which was carried out in a commercial UTN submerged in water.[42] Porous-flow model results are compared with observations of bubbles exiting the inner surface. The UTN was cut in half, sealed at the cut surface, and placed in a water tank. Gas was injected into the bottom of the vertical slit, indicated with dashed lines in Figure 7(a). Note that the UTN in this test was cut in half perpendicular to the cut for the symmetrical half-nozzle domain used in the simulation, as shown in Figure 7(b).

During the experiment, injection pressure was increased slowly, so the gas flow rate increased gradually from zero. The UTN was tilted so that the rising bubbles would not block observation of the "active sites" on the refractory inner surface where bubbles emerge. Because of the good wettability between UTN refractory and water, the hydrostatic pressure along the nozzle, and capillary effects, water may enter some of the pores at the UTN inner surface and block the pore exits. Thus, the bubbling threshold in this test prevents bubbles from exiting regions of low gas pressure.

Both the experiment and the model show a very nonuniform distribution of air exiting the UTN inner surface, as shown in Figure 7. The velocity contours in Figure 8(a) show that gas velocity is greatest at the injection slits, decreases as it diffuses through the refractory, and then increases again when approaching the UTN inner surface. Note much higher velocity exits from the vertical slit on the right side. The velocity vectors in Figure 8(b) show where the surface velocity drops to zero on certain regions of the UTN inner surface far from the injection slits near the bottom. This is due to the pressure threshold enforced by the one-way flow boundary condition. The local pressure in this part of the nozzle was never large enough to overcome the threshold.

It is important to note that the regions where no bubbles are observed in Figure 7(a) match well with the zero-velocity regions in Figure 7(b). There is a slight mismatch near the UTN bottom region where the photo shows gas bubbles coming out from UTN inner surface, while simulation shows no bubbles in that region. One possible explanation for this discrepancy is a nonuniform pore size produced in the UTN refractory during its manufacture: larger pores near the nozzle bottom surface would lower the pressure "bubbling" threshold. The high-velocity regions in Figure 7(b) match with regions where large bubbles are observed in Figure 7(a). Overall, a reasonable match was found between the simulation and the experimental observations, which validates the model, including the one-way-flow pressure boundary condition.

IV. MODEL APPLICATION TO UTN

The validated porous-flow model is next applied to study gas flow distribution in a typical double-slitted UTN shown in Figure 9, under realistic plant operating conditions. A gas line delivers argon into the UTN *via* a system of internal grooves (slits) that distribute the gas into the porous refractory, as pictured in Figure 1. Argon gas is injected into this UTN near the bottom of a vertical slit which feeds two ring-shaped (annular) slits in the upper and lower parts of the nozzle. The vertical slit is needed to reach the upper annular slit, which is inside the tundish bottom and not easily accessible to a gas injection line. During operation, the large temperature gradients in the flowing steel system cause thermal strains that may separate the joints between the refractory parts, such as the UTN and the upper plate. Opening a gap at a joint leads to a local pressure drop and possible gas leakage. The porous-flow model was then applied to investigate gas leakage by comparing two extreme conditions at the UTN bottom surface: one perfectly sealed, with the zero penetrating flow condition (Eq. [13]) (base case), and the other with a large gap, or completely open bottom, with the constant pressure condition (Eq. [14]). Note that in order to be consistent with plant pressure measurements, all the pressure values in this section refer to the gage pressure relative to the ambient pressure of 1 atm (101 kPa).

The computational domain is a radial slice through this UTN, assuming axisymmetry, and the two-dimensional mesh (cylindrical coordinates) contains 5000 4-node quadrilateral cells. They are displayed in Figure 10, together with the boundary conditions. The base case, used in these parametric studies, adopts the temperature-dependent gas viscosity in Eq. [18]. The liquid steel pressure distribution at the refractory-liquid interface determines the overall resistance to gas flow for a given injection pressure. For a slide-gate flow-control system, the UTN is between top of the upper plate (Figure 1) and tundish bottom. Liquid steel flows from the tundish through the UTN, the holes in the three plates, and the submerged entry nozzle (SEN) into the mold. The static pressure distribution from the liquid steel along the inside surface of the UTN, p_l, is reasonably calculated as the hydrostatic pressure with Eq. [17], assuming uniform average vertical cross-flow velocity from the flow rate, and is chosen for the base case, as plotted in Figure 10. The distribution is nearly linear with a maximum pressure of 56 kPa at the UTN bottom just above the upper plate. This base case also adopts a sealed bottom (no leakage at joint), the bubbling pressure threshold, and the one-way flow boundary condition at refractory-liquid interface *via* Eq. [16]. Other operating conditions for the base case are given in Tables II and III.

The temperature field from the heat transfer model is shown in Figure 11. Naturally, temperature increases almost linearly towards the UTN center. The threefold temperature increase causes significant gas expansion, which greatly affects the flow results.

Different boundary conditions on the UTN inner surface were investigated to further demonstrate and evaluate the computational model. Then, parametric studies were conducted to investigate the effects of possible joint (between the UTN and the upper plate) gas leakage, injection pressure, and refractory permeability on the pressure and gas velocity distributions.

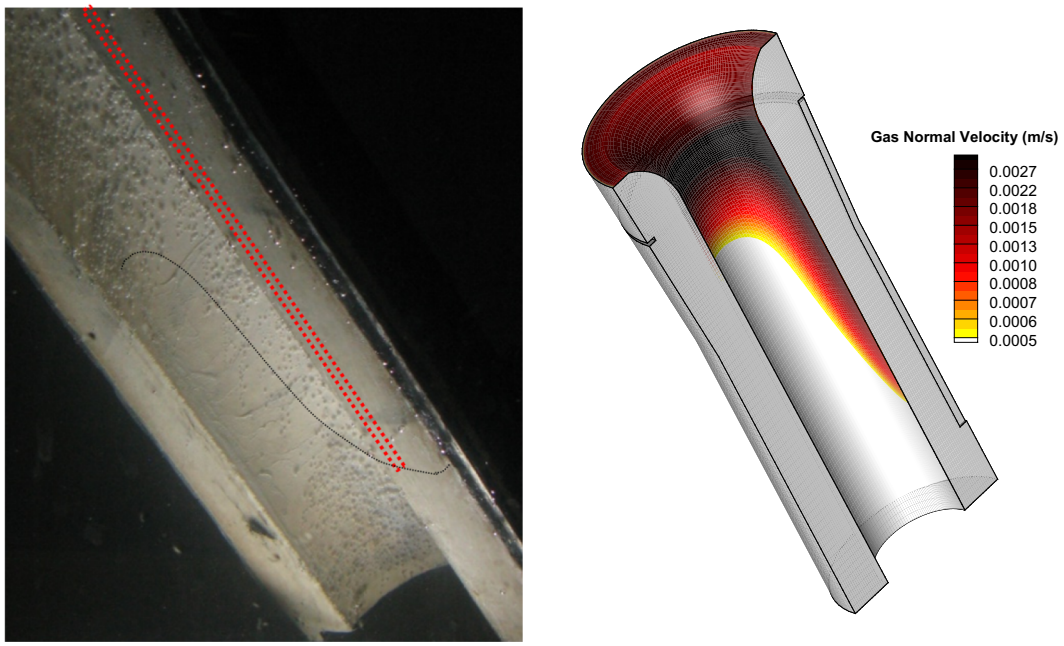

Fig. 7—Comparison between predicted and measured gas flow rate at UTN inner surface.

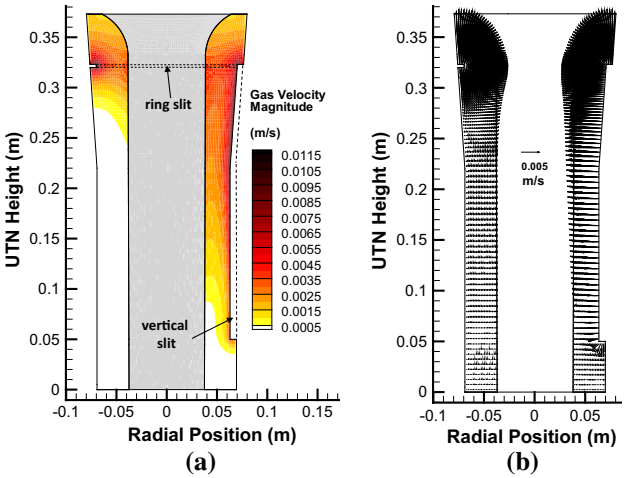

Fig. 8—Gas velocity distribution at symmetry plane (*a*) contours of velocity magnitude; (*b*) velocity vectors.

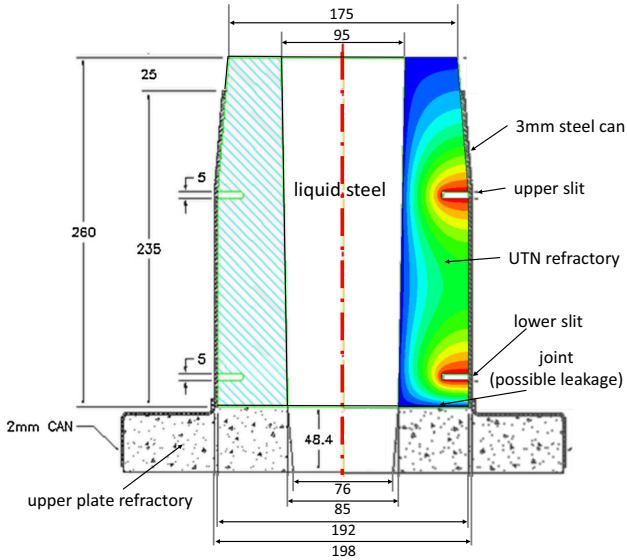

Fig. 9—Schematic of the base case UTN geometry (dimensions in mm).

The gas leakage fraction under different injection pressures was extracted and used to evaluate the performance of this UTN design.

A. *Effect of Pressure Condition at Refractory-Liquid Interface*

Three different pressure distributions in the liquid steel along the refractory-liquid interface are compared to investigate the importance of this boundary condition. Case 1 is the realistic base case, which has a sealed nozzle bottom (no gas leakage at the UTN-plate joint), the linear p_l in Eq. [17], and the gas-bubble pressure threshold, in Eq. [16]. Case 2 is identical to Case 1, but without the bubbling pressure threshold (setting κ to 0 in Eq. [15]). Case 3 has an open bottom, and no pressure threshold for bubble formation at refractory-liquid interface. This case simply assumes constant ambient pressure of 1 atm, (0 Pa gage pressure) for both the interface, p_l, and UTN bottom.

The gas pressure distributions calculated for these three cases are shown in Figure 12. Case 1 (the base case) in Figure 12(a) shows the smallest pressure gradients across the refractory of the three cases. This is because the bubbling threshold and higher liquid hydrostatic pressure combine to increase the resistance to gas flow, which reduces the pressure drop. Case 2 in

Figure 12(b) has larger pressure gradients, especially near the upper slit, due to the lower liquid hydrostatic pressure towards the nozzle top. Case 3 in Figure 12(c) has the steepest pressure gradients.

Velocity distributions exiting the UTN are plotted in Figure 13 for the three cases. A peak in the velocity profile occurs near each of the two slits, simply due to the close proximity to the gas injection slit, which increases the pressure gradient. The realistic base case 1 has the lowest exiting velocities of the three cases, due to the bubbling threshold. Without this threshold, Case 2 has gas exiting velocities increased by ~5 times. Case 3 has the highest exit velocity because the giant pressure gradient from the lower injection slit to the open bottom increases the gas flow everywhere. An additional case, Case 4, is included to show the effect of temperature-dependent gas viscosity in the open bottom case (Case 3), which is small if the temperature for the constant viscosity is chosen to be the liquid metal temperature.

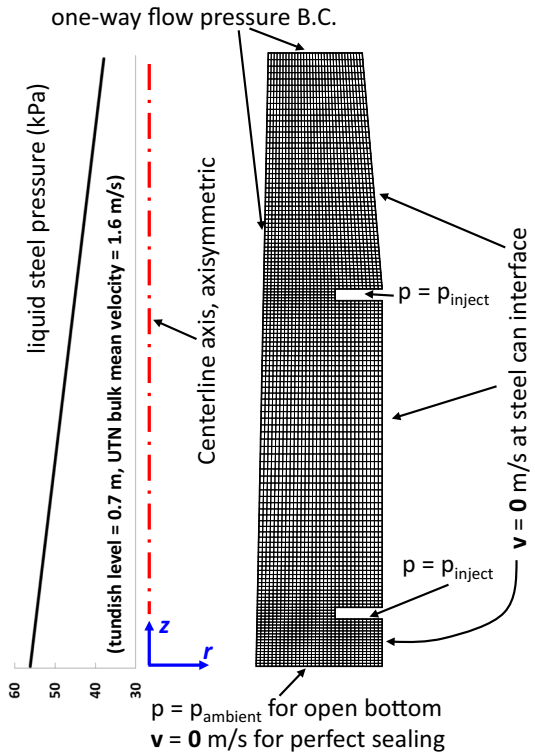

Fig. 10—Computational domain, mesh, and boundary condition.

B. *Effect of One-Way Flow Pressure Boundary Condition*

The velocity field, with and without the proper one-way flow condition is compared in Figure 14 near the UTN bottom, which is open and leaks gas into the joint. Conditions are identical to those of the base case, except for the open bottom, and lack of the one-way flow condition for the case in Figure 14(b). With the one-way flow condition, gas exits the refractory only through the UTN bottom, as shown in Figure 14(a). Without this one-way condition, reverse flow occurs, as shown in Figure 14(b). This unphysical result is caused by the liquid pressure near UTN bottom exceeding the local gas pressure. As discussed before that the location on the UTN inner surface where the pressure boundary becomes a "sealed" wall is embedded as part of the solution from the model. The comparison in Figure 14 indicates that this model is able to seal the regions where liquid pressure is larger than the resolved local gas pressure, and thus prevent the large unphysical "reversed flow" from occurring. These results show that the one-way flow pressure boundary condition is important to realistic model predictions.

C. *Effect of Refractory Thermal Conductivity*

To examine the effect of thermal conductivity on gas flow, alumina–graphite (AG), with a standard conductivity in the base case of this work of 18 W/mK,[37] is compared with doloma, which has a lower conductivity of 2.6 W/mK,[37] owing mainly to its lack of high-conductivity graphite flakes. The temperature distribution in the AG refractory (base Case 1) is shown in Figure 11, and has an UTN outer surface temperature of ~1580 K (~1307 °C). The UTN inner surface temperatures of both cases are almost the same, (~10 K difference) due to the high heat transfer coefficient from the turbulent steel flow. Lowering the conductivity to 2.6 W/mK decreases the outer surface temperature to ~967 K (~694 °C), due to the larger

Table II. Parameters for UTN Heat Transfer Analysis (Base Case)

Heat Transfer, h_{inner} (W/m^2 K)	Coefficients, h_{outer} (W/m^2 K)	Thermal Conductivity, k (W/mK)	Viscosity, μ (Pa s)	Density, ρ (kg/m^3)	Mean Steel Velocity, U (m/s)
25,000	40	18	0.0056	7200	1.6

Table III. Refractory Properties and Casting Conditions in Parametric Study (Base Case)

Tundish Level (m)	Surface Tension, σ (N/m)	Injection Pressure (Gage) (kPa)	Permeability (npm)
0.70	1.157	110	10.1

Ambient Pressure at Tundish Level (Gage) (kPa)	Mean Pore Radius (μm)
0	50

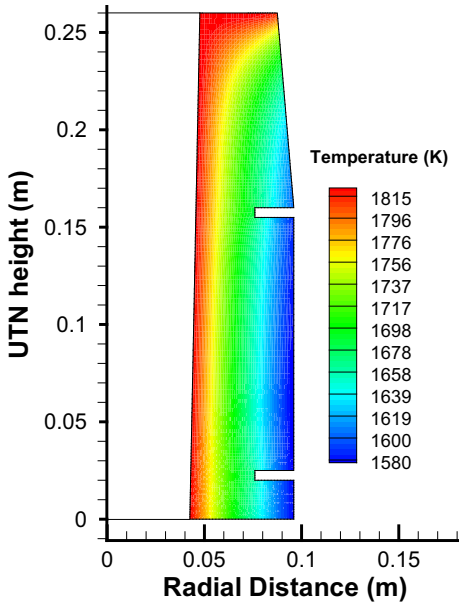

Fig. 11—Temperature distribution across UTN wall (base case).

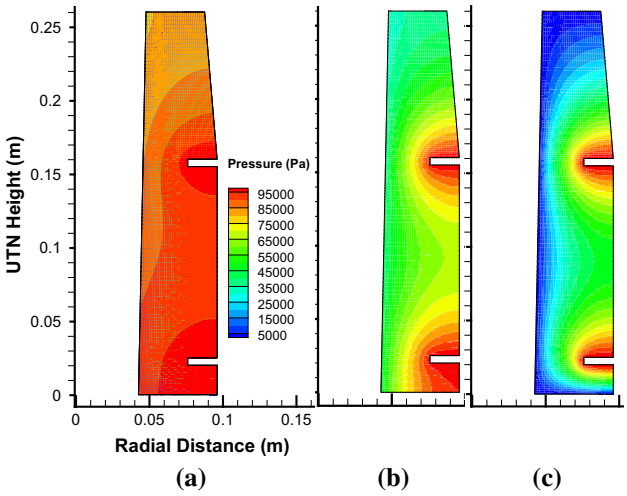

Fig. 12—Effect of liquid steel pressure profile on gage pressure distribution (*a*) Case 1: linear pressure with bubbling threshold; (*b*) Case 2: linear pressure (Fig. 10); (*c*) Case 3: constant pressure.

temperature gradient in the wall. This greater temperature increase from the injection region near the outer wall to the inner wall increases the thermal expansion of the gas, making flow more difficult. More importantly, the lower injection temperature lowers the gas viscosity, so increases the permeability. The net result is higher gas velocity exiting the doloma, for the same pressure drop, as shown in Figure 13. Specifically, Case 5 (2.6 W/mK) has ~30 pct higher gas exit velocity profile than Case 1 (18 W/mK), while retaining a similar distribution down the nozzle.

D. *Effects of Joint Sealing Conditions*

The effect of joint leakage is investigated first by comparing the pressure and velocity distributions of an open bottom case (Figure 15(a)) with the base case (Figure 15(b)), for otherwise identical conditions. Similar pressure and gas velocity distributions are found near the upper slit of the UTN in both cases. However, the distributions near the UTN bottom are very different, as expected. With an open bottom, pressure drops from ~100 kPa to 0 Pa (gage pressure) within a very short distance (from the lower slit to the open bottom), which generates a huge gas velocity exiting the domain. With the one-way flow pressure B.C., the UTN inner surface near the bottom is sealed, preventing any liquid/gas penetration into the porous refractory. Although the injection pressure near the lower slit is higher than the local liquid pressure at the refractory-liquid steel interface, no gas exits that interface near the bottom of the UTN, since the open bottom draws in all the flow and causes the pressure there to drop below the local liquid pressure near the UTN bottom. Gas exits the path of least resistance as shown in the zoomed-in velocity plot in Figure 15(a). With perfect bottom sealing, Figure 15(b) shows how gas can only exit through the UTN inner surface into the liquid steel stream. The corresponding pressure field near the sealed bottom then becomes almost constant, resulting in very low gas velocities. Note that the reference vector scale in Figure 15(b) is increased 10 times for better visualization.

The velocity profiles exiting along the UTN inner surface are plotted for both cases in Figure 16. Flow near the upper slit is almost identical for both cases. However, the flow drops to zero about 80 mm from the UTN bottom (about 1/3 of the total UTN length) in the open bottom case. This is because of the huge pressure gradient created by the imposed ambient pressure at the open bottom, which lowers the flow resistance and deflects the gas flow towards the nozzle bottom.

To quantify and evaluate the performance of the UTN design, the leakage fraction, θ_L, is the amount of the gas leaking away relative to the total gas injected.

$$\theta_L = 1 - \frac{\dot{m}_{in}}{\dot{m}_{total}}, \qquad [22]$$

where $\dot{m}_{in}$ is the gas mass flow rate entering the liquid steel found by integrating the velocity distributions over the UTN inner surface area, and $\dot{m}_{total}$ is the total mass flow rate of the injected gas integrated over the injection-slit surfaces. For the open bottom case in Figure 16, the leakage fraction is 86 pct. This is because a very high flow rate through the leaking open bottom is needed to maintain the pressure gradient. This gas is not wasted because it helps, together with gas injection into the plate, to flush the joint to lessen air aspiration. However, the leakage should be lessened by tighter sealing of the joint, using non-porous refractory, moving the lower gas distribution slit further above the nozzle bottom to lessen the pressure gradient, or other means.

Another type of leakage, possibly caused by thermal expansion differences, is separation of the porous refractory from the outer steel container or "can" that seals the gas distribution slits. This may allow gas from the distribution slits to spread everywhere around the

thin gap that forms between the outer surface of the refractory and the can. A simulation of this situation (not shown) resulted in a higher total gas flow rate with a more uniform distribution of gas exiting from the UTN inner surface than for the other cases in Figure 13. This situation also increases the danger of extra gas leakage from any openings of the thin gap to the ambient atmosphere. It also increases the rate of leakage through the joint at the nozzle bottom, if it is not perfectly sealed.

E. *Effect of Injection Pressure*

Injection pressure drives gas to diffuse through the UTN refractory and is routinely measured during plant operations. A parametric study varying injection pressure was conducted for both the perfectly sealed base case and the same case with an open bottom, with other conditions given in Table III.

Pressure contours for cases with three different injection pressures (90, 99, and 140 kPa) are compared in Figure 17 for the perfectly sealed base case. If the injection pressure is less than a critical minimum injection pressure, then the entire UTN inner surface acts like a "sealed" wall with no gas flowing out, due to the one-way flow boundary condition and pressure threshold at this interface. The pressure and gas velocity distributions for cases chosen near this critical injection pressure are shown in Figure 17(a). Most of the refractory is at an almost uniform pressure near the gas injection pressure of 90 kPa, with almost no pressure gradients. Gas exits only from a tiny region near the very top of the UTN, where the liquid pressure is lowest, and at a negligible flow rate. Increasing the injection pressure to 99 kPa enables gas to exit from the upper half of the UTN inner surface, as shown in Figure 17(b). No gas exits from the lower half because the bubbling threshold is too high, due to the increased liquid hydrostatic pressure towards the nozzle bottom. Further increasing the injection pressure to 140 kPa, gas exits from everywhere on the UTN inner surface, as shown in Figure 17(c).

Figure 18 shows the velocity distributions leaving the UTN inner surface along the axial direction for four different injection pressures (ranging from 90 to 140 kPa) and two different UTN joint sealing conditions (open bottom and perfectly sealed). For a given injection pressure, the velocity profiles for the open bottom and perfectly sealed cases are similar in the upper half of the UTN. Near the UTN bottom, however, the flow drops to 0 for all of the open-bottom cases. This is because the low ambient pressure (1 atm) at UTN bottom is less than the gas pressure threshold at the UTN inner surface. With perfect sealing, for higher injection pressures (*e.g.*, 120 and 140 kPa gage), a second velocity peak is found near the UTN bottom. This is due to high gas velocity exiting regions close to the lower injection slit, as previously discussed.

Figure 19 shows the change of calculated gas mass flow rate at injection slits and that enters liquid steel (flowing through UTN inner surface) with different injection pressures, for both open bottom and perfectly sealed cases, corresponding to the velocity profiles shown in Figure 18. Total injected gas flow rates increase with the injection pressure and are higher in the open bottom case (circles) compared to the perfectly sealed case (squares) for each of the injection pressures studied. The total injected gas flow rate in the perfectly sealed case (squares) increases nonlinearly with the injection pressure close to the gas exiting threshold: for a 9 kPa increase of the injection pressure from 90 to 99 kPa gage, the gas flow rate increases by two orders of magnitude, from ~3×10^{-7} kg/s to ~3×10^{-5} kg/s. As shown also in Figure 19, gas flow rate entering liquid steel in the open bottom case increases with the injection pressure, with a trend similar to that in the perfectly sealed case. As injection pressure increases beyond the threshold, gas flow rate increases in a quasi-linear manner in both the open- and sealed-bottom cases, although this is difficult to see in the log plot. The ratio of gas flow rate entering liquid steel in the open bottom case (triangles) to that in the perfectly sealed case (squares) stays ~0.7 consistently under all injection pressures higher than 99 kPa (above the gas exiting injection pressure threshold). Results with calculated gas leakage fraction following Eq. [22] show that the amount of gas leaking into joint increases from 70 pct with an injection pressure of 140 kPa to ~97 pct with a 99 kPa injection pressure. With a 90 kPa injection pressure in the open bottom case, all of the gas injected into the UTN (~5×10^{-4} kg/s) leaks into the joint.

Figure 19 shows that the gas flow rate lost from the open bottom due to leakage is always very large, exceeding 70 pct. This finding may be specific for the current UTN design, however, which has an annular slit located close to the leaking joint. However, the total gas flow rate increases so much for the leaking joint cases that the gas flow rate exiting into the liquid steel always exceeds 70 pct of the sealed-bottom case, assuming that the pressure can be maintained (at 99 kPa gage or above).

F. *Effect of Permeability*

Specific permeability of the porous refractory indicates its resistance to fluid flow through the spaces in its pore structure. The effect of specific permeability on gas velocity distribution is investigated for both the perfectly sealed bottom base case, and the same case with an open-bottom (leaking joint). Figure 20 shows profiles of the gas velocity exiting along the UTN inner surface for both cases. Figure 21 summarizes the effects of specific permeability on the total gas flow rate exiting the UTN into the liquid steel, based on integrating the velocity profiles in Figure 20. Increasing the specific permeability causes linear increase of the gas exiting velocities from the UTN inner surface (or at the joint in the open-bottom case). The shape of the velocity profile does not change, however, owing to the simple linear relationship between pressure gradient and flow given in Darcy's law Eq. [8] and because varying specific permeability does not change the pressure distribution. This is expected because K_{DS} can be canceled from K_D on both sides of Eq. [9], if it has no spatial variation. Thus, the total gas flow rate and the flow rate entering liquid steel both increase linearly with increasing specific permeability for

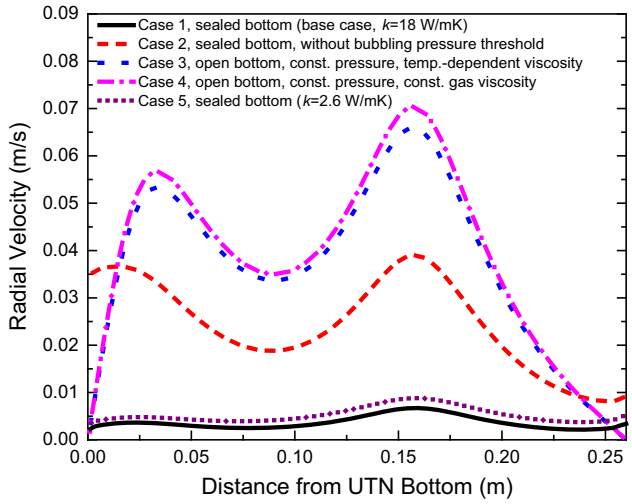

Fig. 13—Radial velocity distribution at UTN inner surface.

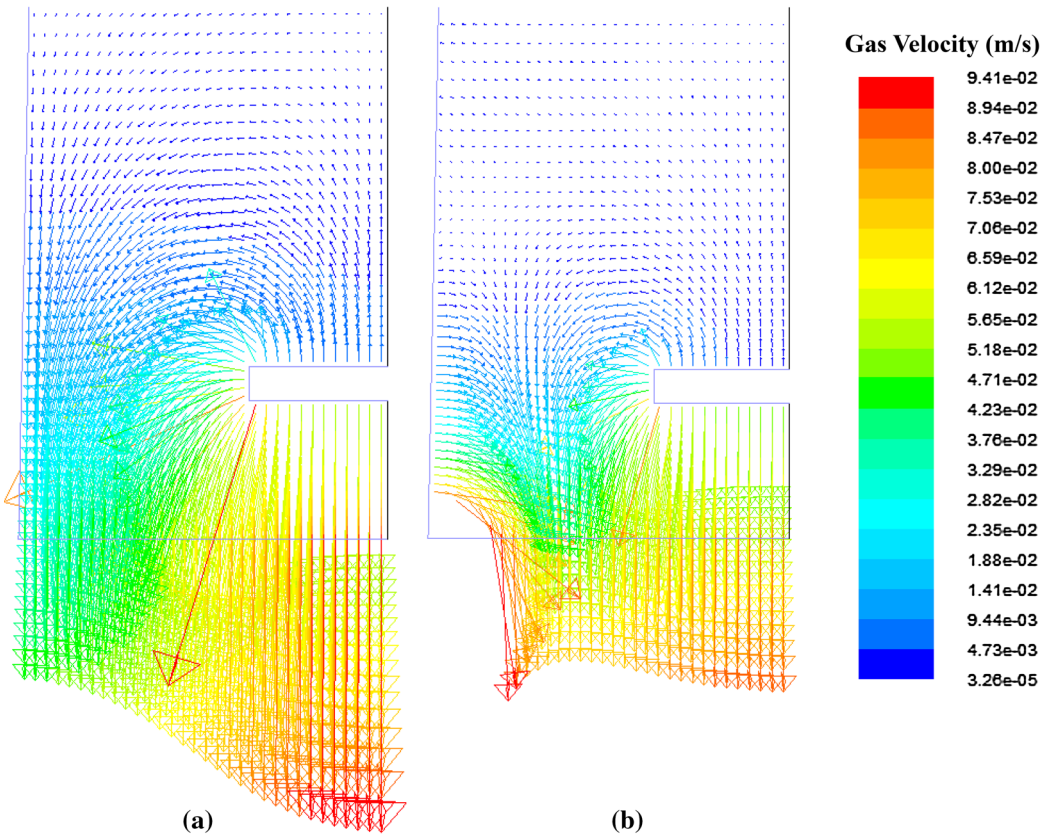

Fig. 14—Velocity near UTN bottom showing effect of boundary conditions.

both perfectly sealed and open-bottom cases, as shown in Figure 21.

With an open-bottom (dashed lines), gas exit velocities all drop to 0 near the bottom of the UTN inner surface. It is easier for the gas to escape from the bottom surface, than to overcome the threshold pressure jump needed to form a bubble at the interface. Figure 21 shows that 86 pct of the gas leaks from the open bottom in Case 2. This large amount does not depend on permeability, but is expected to depend on geometry of the refractory and its slits. Raising the lower distribution slit further away from the UTN bottom joint, or better sealing would lower this leakage fraction.

G. *Practical Applications*

A comprehensive modeling system is proposed to estimate the argon gas flow distribution and initial

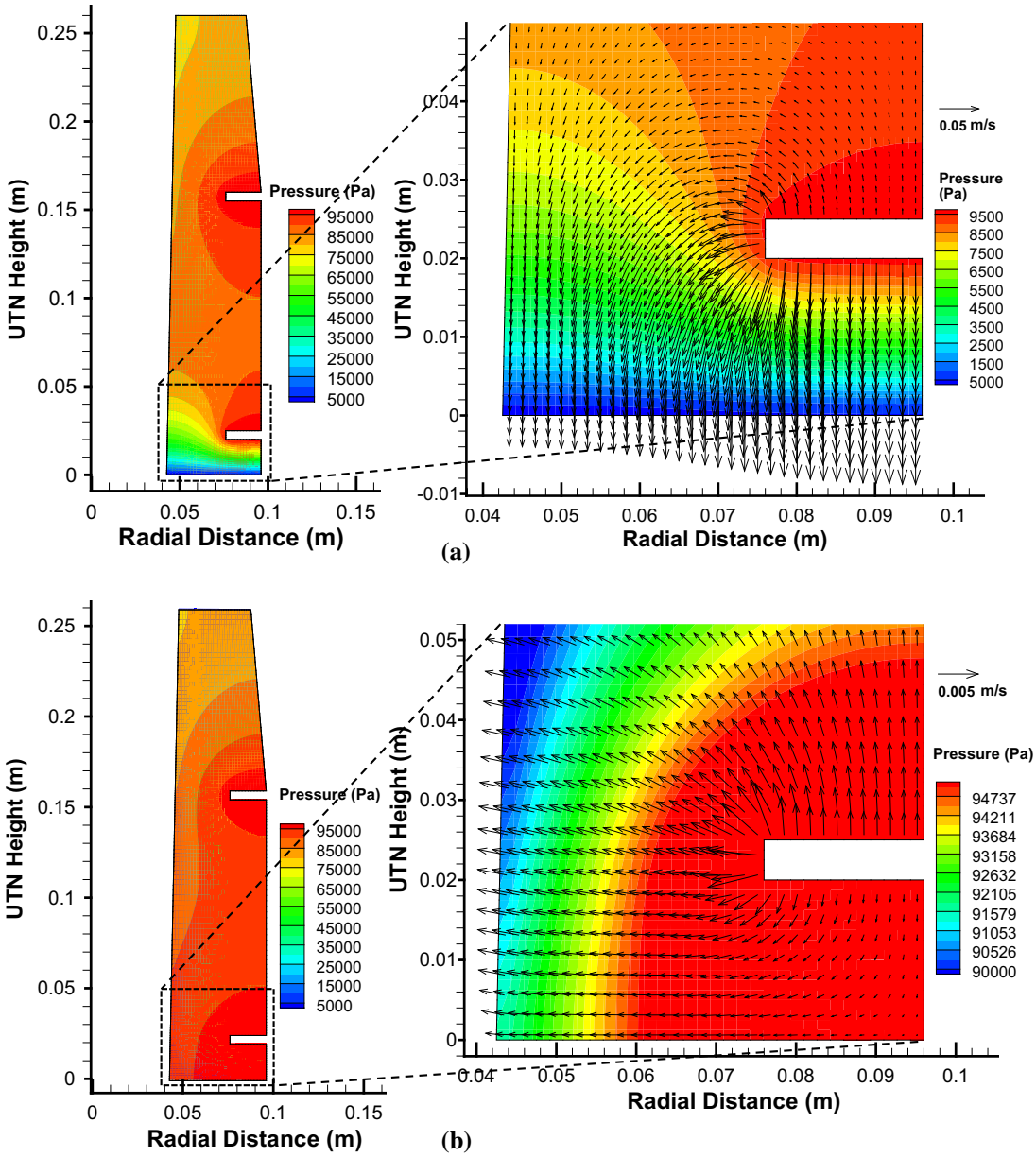

Fig. 15—Pressure (gage) and velocity fields for: (*a*) open bottom case; (*b*) perfectly sealed case.

bubble size entering the liquid steel through nozzles with porous refractories. The porous gas flow model introduced in this work is the first step of this system. This model calculates superficial gas velocity distributions on the UTN inner surface. Next, an empirical model from previous water model bubbling experiments[23] is used to estimate the number density of active sites, based on the local average gas velocity from the first step. Then, the hot gas flow rate from each active site is calculated from the local gas velocity and the local density of active sites. The calculated macroscopic superficial gas velocity is then converted to the physical gas velocity at pore-openings. The gas flow rate through each pore (active site) is input to a two-stage model of bubble formation in downward-flowing liquid[18] to calculate the average bubble size entering into the liquid steel. Finally, a multiphase model of turbulent fluid flow in the nozzle and mold can use these results in realistic simulations to solve practical problems.

1. *Gas leakage detection*

When argon gas is injected during metallurgical processes such as continuous casting, both the volumetric flow rate of gas (usually in SLPM) and the injection pressure are measured and recorded. However, the argon mass flow rate entering the liquid steel can be determined using either one of these two measurements, provided that the specific permeability of the refractory is known. In this work, the measured injection pressure is the preferred boundary condition, because it indicates

the true resistance needed to push the heated gas into the liquid, and drops if there is leakage. The volumetric flow rate, on the other hand, is usually measured upstream before any gas leakage has occurred, so often overestimates the total gas flow entering the molten steel.

Combining the two measurements together enables extra information to be gained about the process. If both the (cold) flow rate and the back pressure are correctly measured, then the actual gas flow rate calculated with the model can be compared with the measured flow rate to quantify how much gas has leaked. An example using this model system to detect gas leakage during continuous casting process can be found elsewhere.[42]

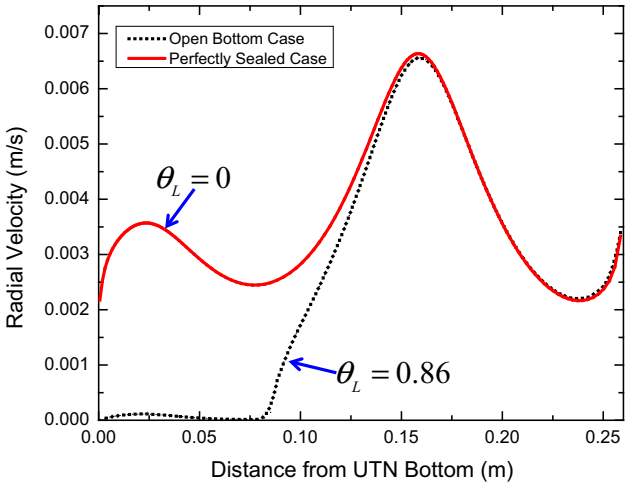

Fig. 16—Effect of gas leakage on radial gas velocity distribution at UTN inner surface.

2. *Design of slide-gate and stopper-rod gas delivery systems*

The liquid pressure distribution over the UTN inner surface in a stopper-rod system is very different from that in the slide-gate system studied in this work. In a stopper-rod system, the gas usually is injected through the stopper-rod tip or the porous refractory of the upper UTN into a very low-pressure region below the gap between the stopper-rod tip and the UTN wall. This causes a high gas-velocity region with high bubble concentrations or even gas pockets, leading to complicated two-phase interactions such as annular flow and other problems.[43] If the upper annular slit is too far above the attachment point of the gas injection line, the needed long vertical slits may

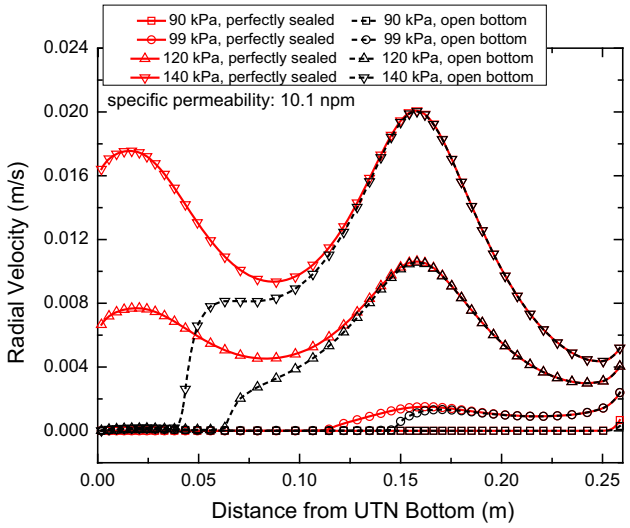

Fig. 18—Effects of injection pressure (gage) and bottom sealing on gas velocity distribution at UTN inner surface.

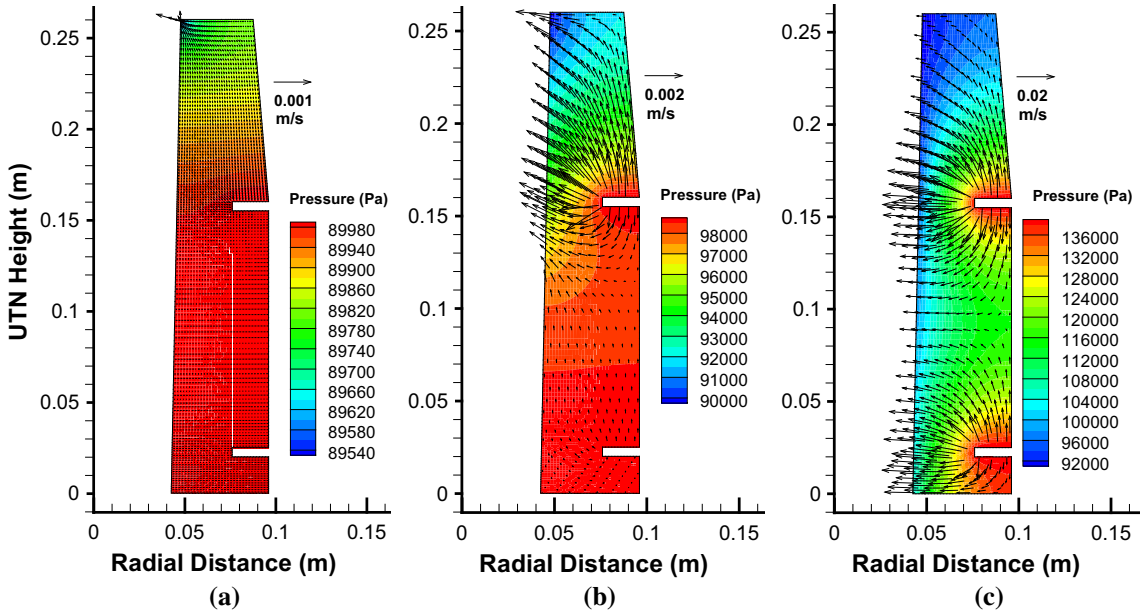

Fig. 17—Effects of injection pressure (gage) on gas velocity distribution in UTN refractory (sealed bottom).

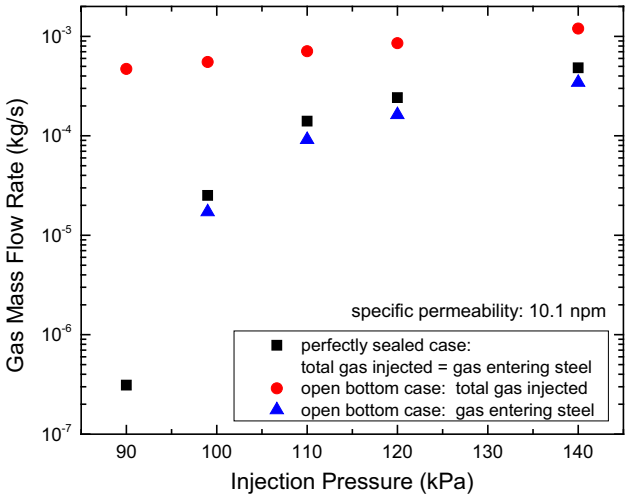

Fig. 19—Effects of injection pressure (gage) on gas flow rate.

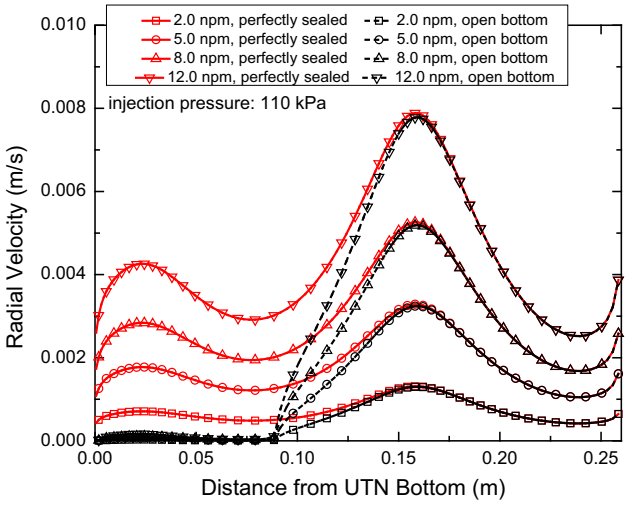

Fig. 20—Effects of permeability on radial velocity distribution.

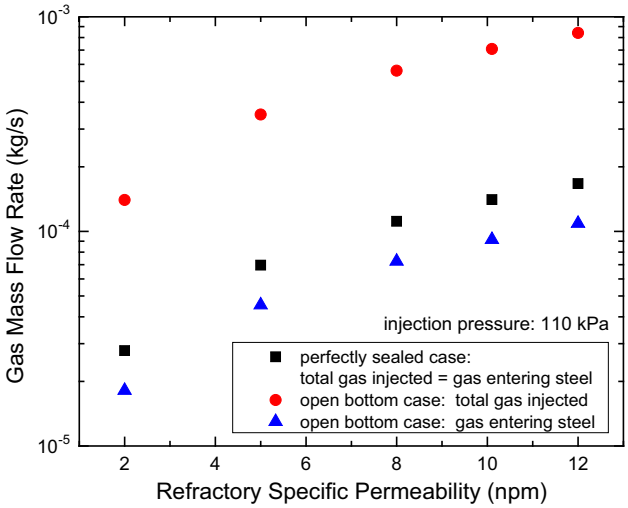

Fig. 21—Effects of permeability on gas mass flow rate.

lead to detrimental asymmetric flow in both the nozzle and mold.[42,44] Careful model calculations of the pressure distribution are needed to predict gas flow behavior and bubble size in this situation, and to aid in redesign of the nozzle geometry.

For slide-gate systems, the results of this work suggest that, the annular gas distribution slit should be located far away from joints at the UTN bottom, to avoid or reduce possible gas leakage from the joint surface. In addition, the optimal location of the gas distribution slits, and the choice of porous/non-porous refractory could be obtained *via* studies using the porous-flow model developed in this work.

V. CONCLUSIONS

A general-purpose model of gas flow through porous refractory has been developed in this work, which includes the pressure threshold at the refractory/liquid metal interface due to gas bubble formation, and a new one-way flow pressure boundary condition to ensure no improper liquid penetration into the refractory. The following conclusions are drawn from initial parametric studies with this new approach:

1. Model validation with 1D analytical solutions shows that both versions of the model correctly account for the effects of thermal expansion of the gas, temperature-dependent gas viscosity, and geometric effects in porous refractory flow problems with high temperature gradients.
2. Model validation with water bubbling experiments shows that the model can accurately simulate gas flow distributions exiting real nozzle refractories, which involve relatively slow gas flow rates, in the regime where Darcy's law holds.
3. A critical injection pressure exists to allow gas bubble formation on the UTN inner surface. Bubbles form and exit from only a fraction of the surface area, where the pressure gradients are highest. This surface area fraction naturally increases with gas injection pressure.
4. The gas velocity profile varies greatly over the UTN inner surface, according to the nozzle geometry and the location of the gas distribution slits. More bubbles exit near to the annular slits, and where the external liquid pressure is lower, owing to the higher pressure gradients.
5. A large amount of gas may escape from the UTN bottom, if the joint leaks. This leakage fraction is predicted to exceed 80 pct for the particular design studied, which has an annular gas distribution slit relatively near to the bottom joint, and no non-porous refractory.
6. Increasing the gas injection pressure naturally increases the total gas flow rate injected. It also decreases the leakage fraction, owing to more gas flowing from the upper slit, for this particular design.
7. Increasing the refractory conductivity increases the total gas flow rate, due to lowering the temperature and gas viscosity injected.

8. The pressure distribution in the refractory is not affected by the specific permeability of the refractory, if it does not vary spatially. Therefore, the total injected gas flow rate increases linearly with increasing specific permeability, while both the shape of the velocity profiles and the leakage fraction stay constant.
9. The seal between the gas distribution slits and the outer-containment steel can is important to the flow distribution. Faulty sealing would lead to increased, more uniform flow distributions but more susceptibility to gas leakage problems.

The new model presented here can serve as the first step of a comprehensive modeling system to simulate gas–metal two-phase flow more accurately. It can provide realistic gas flow distributions in real metallurgical systems, for better estimation of the nonuniform bubble size distributions. Given the measured injection pressure and gas flow rate, this model can also predict the fraction of gas leakage in the real process.

ACKNOWLEDGMENTS

This work was supported by the Continuous Casting Consortium at the University of Illinois. The authors would like to thank Dr. J. Sengupta at ArcelorMittal Dofasco, Dr. H. Yin, and B. Forman at ArcelorMittal Global R&D in East Chicago for their help with the static water bubbling test. The authors also express gratitude to R. Nunnington at Magnesita Refractories for providing data for the parametric studies, and for helpful discussions. Most of all, we thank former graduate student, Zaher Hashisho, now at the University of Alberta, Canada, for initial work on this project.

APPENDIX A. ANALYTICAL SOLUTION FOR 1D TEST PROBLEM

The one-way coupled heat conduction and pressure-source Eqs. [2] and [9] simplify into two ODEs, expressed in cylindrical coordinates as Eqs. [A1] and [A4]. The heat conduction equation,

$$\frac{1}{r}(rT')' = 0, \qquad [A1]$$

has the general solution,

$$T = C_1 \ln r + C_2. \qquad [A2]$$

The two integration constants, C_1 and C_2, are determined from the fixed temperature boundary conditions at the inner (T_1) and outer radius (T_2):

$$C_1 = \frac{T_2 - T_1}{\ln(R_2/R_1)} \quad \text{and} \quad C_2 = \frac{T_1 \ln R_2 - T_2 \ln R_1}{\ln(R_2/R_1)}. \qquad [A3]$$

The 1D gas pressure equation can be expressed as:

$$p'' + \left(\frac{1}{r} - \frac{T'}{T} + \frac{K'_D}{K_D}\right)p' + \frac{p'^2}{p} = 0. \qquad [A4]$$

Equation [A4] was discretized using a central finite-difference scheme and solved with a tri-diagonal matrix algorithm (TDMA), on a 200-node mesh.[42] Equation [A4] can be solved analytically for two special cases: (1) with gas thermal expansion but constant gas viscosity; and (2) without any thermal effects.

With Thermal Expansion and Constant Gas Viscosity

With constant gas viscosity, the Equation [A4] simplifies to:

$$pp'' + p'^2 + pp'\left(\frac{1}{r} - \frac{T'}{T}\right) = 0 \qquad [A5]$$

which has the following positive general solution:

$$p = \sqrt{\frac{C_3}{C_1}(C_1 \ln r + C_2)^2 + 2C_4}. \qquad [A6]$$

Applying Eq. [8] gives the corresponding gas velocity:

$$V_r = -\frac{K_D\sqrt{C_1 C_3}(C_1 \ln r + C_2)}{r\sqrt{(C_1 \ln r + C_2)^2 + \frac{2C_1C_4}{C_3}}}, \qquad [A7]$$

where integration constants C_1 and C_2 are given in Eq. [A3]. Inserting the fixed pressure boundary conditions, at the inner (P_1) and outer radius (P_2) gives:

$$C_3 = \frac{P_2^2 - P_1^2}{T_2^2 - T_1^2}C_1 \text{ and } C_4 = \frac{P_1^2 T_2^2 - P_2^2 T_1^2}{2(T_2^2 - T_1^2)}. \qquad [A8]$$

No Thermal Effects

The simplest scenario ignores both temperature-dependent gas viscosity and gas expansion. Assuming constant viscosity and temperature simplifies Eq. [A4] into:

$$p'' + \frac{p'}{r} = 0 \qquad [A9]$$

which has the pressure solution:

$$p = C_3 \ln r + C_4, \qquad [A10]$$

where,

$$C_3 = \frac{P_2 - P_1}{\ln(R_2/R_1)} \text{ and } C_4 = \frac{P_1 \ln R_2 - P_2 \ln R_1}{\ln(R_2/R_1)}. \qquad [A11]$$

The corresponding gas velocity distribution is: $V_r = -K_D\frac{C_3}{r}$.

REFERENCES

1. B.G. Thomas: *Making, Shaping and Treating of Steel*, A. Cramb, ed., 11th edition, vol. 5, Casting Volume, The AISE Steel Foundation, Pittsburgh, PA, 2003, pp. 1–24.
2. D. Hershey, B.G. Thomas, and F.M. Najjar: *Int. J. Numer. Methods Fluids*, 1993, vol. 17 (1), pp. 23–47.
3. Y. Xie, S. Orsten, and F. Oeters: *ISIJ Int.*, 1992, vol. 32 (1), pp. 66–75.
4. S.T. Johansen, F. Boysan, and W.H. Ayers: *Appl. Sci. Res.*, 1987, vol. 44, pp. 197–207.
5. D. Mazumdar and R.I.L. Guthrie: *ISIJ Int.*, 1995, vol. 35 (1), pp. 1–20.
6. B. Li, H. Yin, C.Q. Zhou, and F. Tsukihashi: *ISIJ Int.*, 2008, vol. 48 (12), pp. 1704–11.
7. L. Wang, H. Lee, and P. Hayes: *ISIJ Int.*, 1996, vol. 36 (1), pp. 17–24.
8. A. Vargas-Zamora, R.D. Morales, M. Diaz-Cruz, J. Palafox-Ramos, and J.D.J. Barreto-Sandoval: *Metall. Mater. Trans. B*, 2004, vol. 35B, pp. 247–57.
9. H. Bai and B.G. Thomas: *Metall. Mater. Trans. B.*, 2001, vol. 32B, pp. 253–67.
10. X. Huang and B.G. Thomas: *Can. Metall. Q.*, 1998, vol. 37 (304), pp. 197–212.
11. T. Shi and B.G. Thomas: Continuous Casting Consortium at University of Illinois at Urbana-Champaign, Report, 2001.
12. H. Yu and M. Zhu: *ISIJ Int.*, 2008, vol. 48 (5), pp. 584–91.
13. V. Singh, S.K. Dash, and J.S. Sunitha: *ISIJ Int.*, 2006, vol. 46 (2), pp. 210–18.
14. B.G. Thomas, X. Huang, and R.C. Sussman: *Metall. Mater. Trans. B*, 1994, vol. 25B, pp. 527–47.
15. R. Gass: Personal Communication, Inland Steel, 1998.
16. M. Iguchi, Y. Demoto, N. Sugawara, and Z. Morita: *ISIJ Int.*, 1992, vol. 32 (9), pp. 998–1005.
17. M. Iguchi, H. Kawabata, K. Nakajima, and Z. Morita: *Metall. Mater. Trans. B*, 1995, vol. 26B, pp. 67–74.
18. H. Bai and B.G. Thomas: *Metall. Mater. Trans. B*, 2001, vol. 32B, pp. 1143–59.
19. S. Ghaemi, P. Rahimi, and D. Nobes: *Phys. Fluids*, 2010, vol. 22, pp. 043305-1–043305-15.
20. N.A. Kazakis, A.A. Mouza, and S.V. Paras: *Chem. Eng. J.*, 2008, vol. 137, pp. 265–81.
21. G. Houghton, A.M. McLean, and P.D. Ritchie: *Chem. Eng. Sci.*, 1957, vol. 7 (1–2), pp. 40–50.
22. B. Bowonder and R. Kumar: *Chem. Eng. Sci.*, 1970, vol. 25, pp. 25–32.
23. G. Lee, B.G. Thomas, and S. Kim: *Met. Mater. Int.*, 2010, vol. 16 (3), pp. 501–06.
24. FLUENT ANSYS Inc. 2007 FLUENT 6.3-Manual (Lebanon, NH).
25. S. Whitaker: *Transp. Porous Media*, 1996, vol. 25, pp. 27–61.
26. S. Ergun: *Chem. Eng. Process*, 1952, vol. 48 (2), pp. 89–94.
27. Y. Lee: ArcelorMittal Inc. Global R&D, Personal Communication, 2011.
28. G.M. Därr and U. Ludwig: *Matériaux Et Constructions*, 1973, vol. 6 (33), pp. 185–90.
29. R.E. Collins: in *Flow of Fluids Through Porous Materials*, C.R. Wilke, ed., Reinhold, Chapman & Hall, London, 1961.
30. G.H. Fancheark and J.A. Lewis: *Ind. Eng. Chem.*, 1933, vol. 25 (10), pp. 1139–47.
31. C.A. Sleicher and M.W. Rouse: *Int. J. Heat Mass Transf.*, 1975, vol. 18, pp. 677–83.
32. P. Wesseling: *Principles of Computational Fluid Dynamics*, Springer, Berlin, 2001. ISBN 7-03-016677-9, pp. 62.
33. T. Young: *Philos. Trans. R. Soc. Lond.*, 1805, vol. 95, pp. 65–87.
34. G. Kaptay, T. Matrushita, K. Mukai, and T. Ohuchi: *Metall. Mater. Trans. B.*, 2004, vol. 35B, pp. 471–86.
35. L. Jimbo, A. Sharan, and A.W. Cramb: *76th Steelmak. Conf. Prof.*, Dallas, TX, 1993, pp. 485–94.
36. R. Dawe and E. Smith: *Science*, 1969, vol. 163, pp. 675–76.
37. R. Nunnington: LWB Refractories, Personal Communication, November 6, 2006.
38. B. van Leer: *J. Comput. Phys.*, 1997, vol. 135 (2), pp. 229–48.
39. S.V. Patankar: *Numerical Heat Transfer and Fluid Flow*, Hemisphere, Washington, DC, 1980.
40. S.R. Mathur and J.Y. Murthy: *Numer. Heat Transfer Part B*, 1997, vol. 31 (2), pp. 195–215.
41. S. Achaya, B.R. Baliga, K. Karki, J.Y. Murthy, C. Prakash, and S.P. Vanka: *J. Heat Transf.*, 1996, vol. 129 (7), pp. 407–24.
42. R. Liu and B.G. Thomas: *Proc. AISTech 2012 Steelmak. Conf.*, Atlanta, GA, 2012, pp. 2235–46.
43. M. Burty, M. Larrecq, C. Pusse, and Y. Zbaczyniak: *Revue de Metallurgie. Cahiers D'Informations Techniques*, 1996, vol. 93 (10), pp. 287–92.
44. J. Sengupta and S.D. Chung: *Proc. AISTech 2014 Steelmak. Conf.*, Indianapolis, IN, 2014, pp. 1857–64.